remote sensing

MDPI

Article

Inversion of Land Surface Temperature and Prediction of Geothermal Anomalies in the Gonghe Basin, Qinghai Province, Based on the Normalized Shade Vegetation Index

Zongren Li [1,2,3], Rongfang Xin [1,2,3,*], Xing Zhang [1,2,3], Shengsheng Zhang [4], Delin Li [1,2,3], Xiaomin Li [1,2,3], Xin Zheng [5] and Yuanyuan Fu [5]

[1] Institute of Geological Survey of Qinghai Province, Xining 810012, China; 18697238339@163.com (Z.L.); 18997121126@163.com (X.Z.); 13389755881@163.com (D.L.); 15309718236@163.com (X.L.)
[2] Qinghai Remote Sensing Big Data Engineering Technology Research Center, Xining 810012, China
[3] The Northern Qinghai-Tibet Plateau Geological Processes and Mineral Resources Laboratory, Xining 810012, China
[4] Qinghai Institute of Hydrogeological, Engineering Geological, and Environmental Geological Surveys, Xining 810001, China; 15809711951@163.com
[5] School of Geography and Information Engineering, China University of Geosciences, Wuhan 430074, China; 2971372855@cug.edu.cn (X.Z.); fuyuanyuan@cug.edu.cn (Y.F.)
* Correspondence: qhxrf@163.com

Highlights

What are the main findings?

- The novel Normalized Shaded Vegetation Index (NSVI) effectively resolves spectral confusion in sloped terrain and enhances the accuracy of surface emissivity calculations.
- Combining NSVI with radiation-transfer-based Land Surface Temperature (LST) inversion techniques yields high-precision LST estimates.

What is the implication of the main finding?

- This framework provides a replicable, efficient solution for geothermal exploration in complex topography regions like the Gonghe Basin, with potential for broader application across the Tibetan Plateau.
- By precisely identifying high-potential geothermal zones in the Gonghe Basin, it optimizes exploration efforts, supports targeted resource development, and reduces exploration uncertainty.

check for updates

Academic Editor: Donglian Sun

Received: 5 September 2025
Revised: 15 October 2025
Accepted: 16 October 2025
Published: 20 October 2025

Citation: Li, Z.; Xin, R.; Zhang, X.; Zhang, S.; Li, D.; Li, X.; Zheng, X.; Fu, Y. Inversion of Land Surface Temperature and Prediction of Geothermal Anomalies in the Gonghe Basin, Qinghai Province, Based on the Normalized Shade Vegetation Index. *Remote Sens.* **2025**, *17*, 3485. https://doi.org/10.3390/rs17203485

Copyright: © 2025 by the authors. Licensee MDPI, Basel, Switzerland. This article is an open access article distributed under the terms and conditions of the Creative Commons Attribution (CC BY) license (https://creativecommons.org/licenses/by/4.0/).

Abstract

Against the backdrop of global energy transition, geothermal energy has emerged as a critical renewable resource, yet its exploration remains challenging due to uneven subsurface distribution and complex surface conditions. This study pioneers a novel framework integrating the Normalized Shaded Vegetation Index (NSVI) with radiative transfer-based land surface temperature inversion to detect geothermal anomalies in the Gonghe Basin, Qinghai Province. Using multi-source remote sensing data (GF5 B AHSI, ZY1–02D/E AHSI, and Landsat 9 TIRS), we first constructed NSVI, achieving 97.74% classification accuracy for shadowed vegetation/water bodies (Kappa = 0.9656). This effectively resolved spectral mixing issues in oblique terrain, enhancing emissivity calculations for land surface temperature retrieval. The radiative transfer equation method combined with NSVI-derived parameters yielded high-precision land surface temperature estimates (RMSE = 2.91 °C; R^2 = 0.963 against Landsat 9 products), revealing distinct thermal stratification: bright vegetation (41.31 °C) > shadowed vegetation (38.43 °C) > water (33.56 °C). Geothermal anomalies were identified by integrating temperature thresholds (>45.80 °C),

7 km fault buffers, and concealed Triassic granite constraints, pinpointing high-potential zones covering 0.12% of the basin. These zones are concentrated in central Gonghe, northern Guinan, and central-northern Guide counties. The framework provides a replicable solution for geothermal prospecting in topographically complex regions, with implications for optimizing exploration across the Gonghe Basin.

Keywords: geothermal anomalies; normalized shaded vegetation index; thermal infrared remote sensing; land surface temperature; the Gonghe Basin

1. Introduction

Against the backdrop of dwindling traditional fossil fuel resources and the accelerating pace of global energy transition, the role of renewable energy in the global energy system has become increasingly prominent [1,2]. Geothermal energy [3], solar energy [4], wind energy [5], tidal energy [6], and hydropower [7], as core components of green new energy, have seen their share in the global energy structure steadily increase, sparking extensive academic research and practical exploration. By the 1990s, geothermal resources had become a widely recognized and accessible clean and renewable energy source, attracting significant international attention and driving intensified development efforts [8]. China possesses abundant geothermal resources, accounting for approximately one-sixth of the world's total geothermal reserves, with significant potential for further development and utilization [9]. However, the formation and spatial distribution of geothermal resources are significantly influenced by specific geological structural characteristics [10]. Given the highly uneven distribution of global geothermal resources, this inevitably poses a major challenge to the widespread and intensive exploitation of geothermal resources worldwide [11]. Therefore, it is essential to conduct systematic geothermal surveys, scientifically evaluate geothermal advantage zones, and prioritize suitable exploration target areas.

Identifying geothermal anomaly zones, particularly medium-temperature anomalies (specifically high-temperature anomalies exceeding the surface temperatures of other objects on the ground), is a critical prerequisite for mapping geothermal resource distributions and advancing related research and practical applications [12]. This process is a complex interdisciplinary system that integrates various methods. The methods for identifying geothermal anomalies include thermal infrared (TIR) remote sensing technology [13], geophysical exploration techniques [14], geochemical analysis methods [15], mathematical statistical models, and spatial analysis techniques [16]. TIR remote sensing technology offers significant advantages in terms of efficiency and cost-effectiveness due to its extensive information content, high detection accuracy, and ability to rapidly identify anomalies on a large scale with minimal constraints from ground conditions [17]. It effectively delineates land surface temperature anomaly zones, providing new perspectives and technical approaches for the exploration and development of geothermal resources [18].

Shadows are one of the fundamental characteristics of remote sensing imagery [19]. They are darker regions formed on images due to oblique lighting and terrain obstruction, and are divided into umbra and penumbra. The umbra refers to the dark regions of an object not illuminated by the sun, while the penumbra refers to the shadows cast by an object illuminated by the sun [20]. Shadows have low spectral reflectance values, contain little information, and are difficult to distinguish, which can interfere with land classification and image matching, thereby limiting the application of remote sensing imagery in various fields [21]. Shadow detection helps restore the original information of land features, improves the quality of remote sensing imagery, and plays an important role

in fields such as precision agriculture and urban construction [22]. How to better identify shadows and improve classification accuracy has become one of the research hotspots in this field. Xu et al. [23] developed the Shaded Vegetation Index (SVI) and further refined it into the Normalized Shaded Vegetation Index (NSVI). This index amplifies spectral differences between objects, enabling effective distinction between vegetation and water bodies in shaded areas. Badgley et al. [24]'s expression for estimating total primary productivity aligns with the SVI, and the NSVI is currently used to eliminate shadows from apple tree canopies in multispectral imagery, further highlighting the practicality of the SVI and NSVI developed by Xu et al. [23]. The reflectance thresholds for umbra and penumbra were defined based on empirical analysis of spectral curves, where umbra corresponds to darker shadows (lower reflectance in NIR), and penumbra represents transitional shadows [23].

This paper takes the Gonghe Basin as the study area and integrates multi-source data, such as thermal infrared remote sensing and geological structure, to construct a method for inferring a regional-scale land surface temperature based on the normalized shadow vegetation index (NSVI). This method is used to detect potential geothermal resource areas in the Gonghe Basin, providing a theoretical basis for the development of its geothermal resources.

2. Materials and Methods

2.1. Study Area

The Gonghe Basin is located in the northeastern part of Qinghai Province, China, within the tectonic subsidence zone along the northeastern margin of the Qinghai–Tibet Plateau (Figure 1). It serves as a crucial tectonic transition zone between the Qinghai–Tibet Block and the Qilian Orogenic Belt to its north and the Xixi Ling Orogenic Belt to its east. The geographical coordinates of the Gonghe Basin are approximately between 35°30′ and 37°00′ north latitude and 98°30′ and 101°30′ east longitude. The Gonghe Basin is surrounded by high mountains, forming a relatively independent and closed topographical unit. The region exhibits intense tectonic activity, with well-developed faults and frequent geothermal activity, creating favorable conditions for the migration and accumulation of geothermal fluids. Existing studies have shown that multiple medium-to-high-temperature geothermal fields have been discovered in areas such as Qabqa Town and Guide County, indicating that the Gonghe Basin holds promising prospects for geothermal resource development [25]. Currently, the development of geothermal resources in the Gonghe Basin is still in its initial stages, with insufficient utilization of geothermal resources, indicating a broad development prospect.

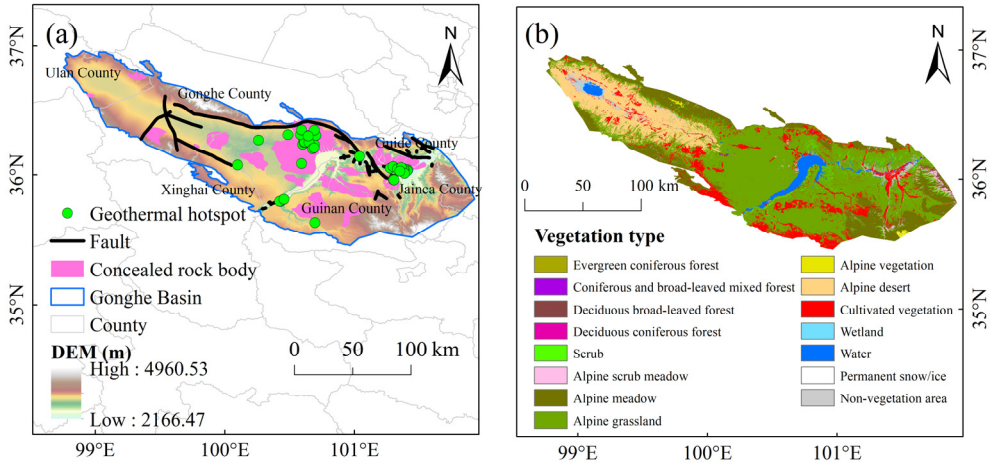


Figure 1. Study Area. (**a**) Location and elevation of the Gonghe Basin, along with the distribution of geothermal hotspots, fault, and concealed rock body; (**b**) Vegetation types in the Gonghe Basin.

From a tectonic perspective, the Gonghe Basin is an inland graben basin formed under the control of a composite tectonic structure of strike-slip and compression during the Cenozoic era, with a complex geological tectonic background [26]. The basin itself is controlled by the South Qilian Fault, the Kunlun Fault, and others. The basin's basement is primarily composed of Indosinian Middle to Late Triassic granites and Paleozoic metamorphic rock sequences, with overlying layers dominated by thick Quaternary clastic sediments. The Gonghe Basin formed during the Cenozoic era, with stratigraphy including discontinuous Jurassic, Cretaceous, Miocene, and Pliocene deposits, overlain by Quaternary sediments. Mesozoic intrusions are exposed due to metamorphic peeling in fault zones. Fault activity within the basin is frequent, providing pathways for the transfer of thermal energy from deeper to shallower zones.

The Gonghe Basin spans geological strata from Precambrian metamorphic rocks to Cenozoic formations. Among these, Mesozoic clastic rocks, Cenozoic red beds, and magmatic intrusions along fault zones are widely distributed, exhibiting high radioactive heat generation capacity and serving as an important component of the region's deep heat sources [27]. Late Triassic granites were intruded under compressional conditions, while Cenozoic faulting reflects transtensional dynamics, indicating different geodynamic settings. Cenozoic volcanic rocks and the sedimentary sequence of the graben basin provide favorable thermal reservoir and cap rock conditions for the storage and migration of thermal fluids.

2.2. Datasets

2.2.1. Remote Sensing Data

The Gaofen-5 (GF-5) is equipped with the Advanced Hyperspectral Imager (AHSI) visible shortwave infrared hyperspectral camera, which is the first satellite-borne hyperspectral camera in the world to combine wide coverage, a wide spectral range, and high quantification levels [28]. It is of great significance in the fields of water environment remote sensing, ecological environment remote sensing, solid waste remote sensing, and mineral identification and mapping. The number of spectral bands is 330, with a spatial resolution of 30 m. The ZiYuan-1–02D/E (ZY1–02D/E) satellite is the first civilian high-spectral business satellite successfully launched into orbit on 12 September 2019 [29]. It is equipped with a visible near-infrared camera and a high-spectral camera, with a spatial resolution of 30 m, with 166 spectral channels. The experimental images used in this study are 23 GF5B and ZY1–02D/E AHSI images covering the Gonghe Basin in 2023 (https://data.cresda.cn, accessed on 1 July 2025) (Tables 1 and 2). The experimental images underwent preprocessing, including radiometric calibration and atmospheric correction.

We also utilized three Landsat 9 satellite remote sensing imagery datasets covering the Gonghe Basin in August 2024 (LC09-L1TP), as well as official land surface temperature products (Collection 2 Level-2) (https://earthexplorer.usgs.gov/, accessed on 1 July 2025). TIRS data were used to calculate the land surface temperature of the region. Official land surface temperature products were used for result validation. To ensure precise comparison between different satellite products, all remote sensing data (GF5B AHSI, ZY1–02D/E AHSI, and Landsat 9 TIRS) were rigorously co-registered to a common geographic coordinate system (WGS84 UTM Zone 47N) using a polynomial transformation model with nearest-neighbor resampling. The root mean square error (RMSE) of the co-registration was controlled within 0.3 pixels (9 m). Subsequently, all datasets were resampled to a consistent spatial resolution of 30 m using the bilinear interpolation method to match the Landsat 9 grid for accurate pixel-to-pixel comparison.

Table 1. Materials used in this study.

Satellite/Sensor	Data Type	Bands Used	Spatial Resolution	Temporal Coverage	Data Source/Product	Purpose
GF-5B AHSI	Hyperspectral Imagery	VNIR-SWIR (330 bands)	30 m	2023	https://data.cresda.cn, accessed on 1 July 2025	NSVI calculation, Land cover classification
ZY1–02D/E AHSI	Hyperspectral Imagery	VNIR-SWIR (166 bands)	30 m	2023	https://data.cresda.cn, accessed on 1 July 2025	NSVI calculation, Land cover classification
Landsat 9 TIRS	Thermal Infrared	Band 10, 11	100 m (resampled to 30 m)	August 2024	LC09-L1TP	LST inversion input
Landsat 9 LST	Land Surface Temperature	-	30 m	August 2024	Collection 2 Level-2	Cross-validation
Geological Data	Fault lines, Rock masses	-	-	-	Qinghai Provincial Bureau	Geothermal targeting constraints

Table 2. Details of remote sensing image data in this study.

Serial Number	Satellite Type	Imaging Date	Cloud Coverage (%)	Imaging Time
1	GF5B AHSI	2023–04–11	0	daytime
2	GF5B AHSI	2023–04–18	0.1	daytime
3	GF5B AHSI	2023–04–18	0	daytime
4	GF5B AHSI	2023–04–25	0	daytime
5	GF5B AHSI	2023–04–25	0.1	daytime
6	GF5B AHSI	2023–05–02	9.2	daytime
7	GF5B AHSI	2023–05–02	9.6	daytime
8	GF5B AHSI	2023–06–29	2.4	daytime
9	GF5B AHSI	2023–07–22	8.1	daytime
10	GF5B AHSI	2023–07–29	2.1	daytime
11	GF5B AHSI	2023–08–28	3.9	daytime
12	GF5B AHSI	2023–09–04	0.2	daytime
13	GF5B AHSI	2023–09–04	0.2	daytime
14	GF5B AHSI	2023–10–02	0.3	daytime
15	ZY01E AHSI	2023–11–26	6	daytime
16	ZY01F AHSI	2023–08–24	10	daytime

2.2.2. Geothermal Geological Data

From the original data obtained from the Qinghai Provincial Bureau of Hydrogeological, Engineering Geological, and Environmental Geological Surveys, including geological maps, geological structural maps, geothermal geological maps, and Tertiary hydrogeochemical type maps of the Gonghe Basin, vector data for fault distribution lines and concealed rock mass surfaces were extracted using MapGIS (Version 6.7) and ArcGIS (Version 10.2) data processing software.

The geothermal hotspot data used in this study were obtained from the geothermal geological map of the Gonghe Basin provided by the Qinghai Provincial Bureau of Hydrogeological, Engineering Geological, and Environmental Geological Surveys. The data were vectorized using ArcGIS and extracted into a point vector data format, resulting in 40 valid geothermal hotspots, including hot springs and hot wells identified through field surveys.

2.3. Construction of Normalized Shadow Vegetation Index

Shadows are a major cause of the "same object, different spectral signature" and "different objects, same spectral signature" phenomena in remote sensing images [20]. By establishing the NSVI, it is possible to effectively detect vegetation in shadowed areas. There are significant differences in reflectance between vegetation in bright areas, vegetation in shadowed areas, and water bodies in the infrared band. NDVI is sensitive to vegetation changes, so multiplying NDVI by the near-infrared band enhances the spectral differences between objects, resulting in SVI [23], whose expression is:

$$\mathrm{SVI} = \mathrm{NDVI} \times \mathrm{NIR} = \frac{(\mathrm{NIR} - \mathrm{R}) \times \mathrm{NIR}}{\mathrm{NIR} + \mathrm{R}} \quad (1)$$

In the formula, *NIR* is the near-infrared band reflectance; *R* is the red band reflectance. To maintain consistency with the *NDVI* scale, *SVI* is normalized to form *NSVI*, whose expression is:

$$\mathrm{NSV\,I} = \frac{\mathrm{SVI} - \mathrm{SVI_{min}}}{\mathrm{SVI_{max}} - \mathrm{SVI_{min}}} \quad (2)$$

In the formula, SVI_{max} is the maximum value of *SVI*; SVI_{min} is the minimum value of *SVI*. According to existing research, the optimal bands selected for GF5B are B86 (781 nm) and B99 (864 nm) [30], while the optimal bands selected for ZY1–02D/E are B32 (808 nm) and B73 (864 nm) [23]. All AHSI imagery was first radiometrically calibrated to convert digital numbers to radiance. Surface reflectance was then retrieved using the FLAASH (Fast Line-of-sight Atmospheric Analysis of Spectral Hypercubes) model to remove atmospheric effects (e.g., aerosols, water vapor) before calculating NSVI. A DEM was integrated for topographic correction, including beta and slope adjustments, to minimize terrain-induced errors in LST inversion.

NSVI is a dimensionless index scaled between 0 and 1. Similar to NDVI, its magnitude indicates the relative abundance of vegetation within a pixel, but with significantly improved sensitivity in topographically shaded areas. A value near 1 indicates high vegetation cover (whether in sunlit or shaded conditions), while a value near 0 indicates non-vegetated surfaces like bare soil or water.

2.4. Land Surface Temperature Inversion

We use the radiation transfer equation method to invert surface temperature because of its universality [31]. The radiative transfer equation is specifically applied to Landsat 9 TIRS bands (B10 and B11) for LST inversion, while NSVI is derived from AHSI data for emissivity correction. The thermal radiation received by the remote sensor mainly consists of three parts: thermal radiation from the surface that is attenuated by the atmosphere and then received by the remote sensor; thermal radiation from the atmosphere that is reflected by the surface and then attenuated by the atmosphere before being received by the remote sensor; and thermal radiation from the surface that is reflected by the atmosphere and then received by the remote sensor. Therefore, the formula for calculating the surface thermal radiation received by the sensor is as follows:

$$\begin{aligned} \mathrm{B_i(T_i)} = \tau_\mathrm{i}(\theta) \times [\varepsilon_\mathrm{i} \times \mathrm{B_i(T_s)} + (1 - \varepsilon_\mathrm{i}) \times \mathrm{L_i} \downarrow] \\ + \mathrm{L_i} \uparrow \end{aligned} \quad (3)$$

In the equation, T_i is the brightness temperature of channel *i*; T_s is the land surface temperature; ε_i is the surface emissivity; $\tau_i(\theta)$ is the atmospheric transmittance from the ground to the remote sensor for channel i at the remote sensor's viewing angle θ; $B_i(T_i)$ is the radiation intensity received by the remote sensor; $B_i(T_s)$ is the blackbody radiation intensity when the land surface temperature is T_s; $L_i\downarrow$ and $L_i\uparrow$ are the downward and

upward radiation intensities of the atmosphere, respectively. The atmospheric parameters in Equation (3), including atmospheric transmittance (τ_i), upwelling radiance ($Li\uparrow$), and downwelling radiance ($Li\downarrow$), were directly extracted from the metadata files (MTL.json) of the USGS Landsat 9 Level-2 products (https://www.usgs.gov/landsat-missions/landsat-collection-2-level-2-science-products, accessed on 1 July 2025). For each scene, the parameters corresponding to the thermal infrared bands (B10 and B11) were used. This approach leverages the well-validated atmospheric correction algorithm employed by USGS, ensuring accuracy and consistency with the official data processing stream. The land surface temperature is obtained using the inverse of Planck's law:

$$T_s = \mathrm{K}_2 / \ln[\mathrm{K}_1 / B(T_s) + 1] - 273.15 \quad (4)$$

In the formula, K_1 and K_2 are constants that can be found in the metadata MTL file.

The surface emissivity ratio is the ratio of the radiance emitted by an object to that emitted by a blackbody at the same temperature and wavelength. Its value is closely related to the material structure of the surface. The surface emissivity ratio is calculated using the NDVI threshold method proposed by Julien & Sobrino [32]. In this study, the improved NSVI is used to replace NDVI for calculating the surface emissivity ratio. The substitution of NDVI with NSVI for emissivity calculation is motivated by the need to address spectral mixing in shaded terrain. While NDVI is sensitive to vegetation abundance, it fails to discriminate between shaded vegetation and water bodies due to reduced reflectance in shadowed areas. This leads to biased emissivity estimates in mixed pixels, particularly in oblique terrains where shadows are prevalent. NSVI, by amplifying near-infrared differences and normalizing the SVI scale, enhances spectral separability between land cover types (Table 1), thereby improving emissivity accuracy. This correction is critical for reducing LST inversion errors in fault-controlled basins like Gonghe, where shadowing exacerbates spectral ambiguity. The surface albedo is calculated as:

$$\varepsilon = 0.004 p_v + 0.986 \quad (5)$$

$$\mathrm{p_v} = (\mathrm{NSVI} - \mathrm{NSVI_{soil}}) / (\mathrm{NSVI_{veg}} - \mathrm{NSVI_{soil}}) \quad (6)$$

In the formula, p_v represents vegetation coverage; $NSVI_{soil}$ represents the $NSVI$ value of bare land; $NSVI_{veg}$ represents the NSVI value of vegetation. When $NSVI \geq 0.22$ in this study, the pixel is considered to be completely covered by vegetation, and the surface reflectance is taken as 0.986.

2.5. Prediction of Potential Geothermal Anomaly Zones

There are currently 40 known active geothermal hotspots in the study area, including hot springs and geothermal wells identified through field surveys. To investigate the relationship between land surface temperature and geothermal hotspots, land surface temperature data were extracted using ArcGIS software. Qin et al. [33] found that the temperature in geothermal anomaly zones in the Tengchong region of Yunnan Province was approximately 4–10 Kelvin (K, 1 °C = 274.15 K) higher than in background areas; Darge et al. [34] found that the land surface temperatures in the high-temperature anomaly zones of the Ethiopian Rift Valley were approximately 3–9 K higher than those in the background zones. The inversion results for the study area were classified to facilitate further extraction of geothermal anomaly zones. In this study, land surface temperatures higher than the existing geothermal outcrop points in the study area were selected as geothermal anomaly zones, and non-geothermal influence areas were further excluded.

Geothermal activity is controlled by geological structures. Specifically, actual geothermal zones are typically distributed around faults and aligned with the direction of active

faults, or distributed around the intersection of multiple faults [35]. These two points are important criteria for distinguishing between genuine and false geothermal zones. A concealed rock mass refers to a rock mass structural unit buried beneath the Earth's surface that is difficult to directly observe through conventional geological surveys. It typically includes magmatic intrusions in the deep crust and faulted rock masses. Subsurface rock bodies typically possess high thermal storage capacity, enabling them to effectively store and conduct geothermal energy [36]. The structural fractures and faults surrounding subsurface rock bodies provide favorable pathways for the migration of underground thermal fluids. The distribution of subsurface rock bodies is often correlated with the spatial distribution of geothermal points.

The 7 km fault buffer distance was selected based on regional geological characteristics and prior studies of geothermal systems in similar rift basins. In the Gonghe Basin, fault systems (e.g., the South Qilian Fault) serve as primary conduits for deep hydrothermal fluid migration, with geothermal activity typically concentrated within 5–10 km of major faults due to heat dissipation and fluid pathways [35]. Specifically, Zhang et al. [37] observed that >80% of geothermal fields in the Tibetan Plateau reside within 5 km of major faults, while Darge et al. [34] used a 10 km buffer for the Ethiopian Rift. Our analysis of known geothermal hotspots in the Gonghe Basin (n = 40) revealed that 87% (35/40) are located within 7 km of fault zones, confirming this distance as optimal for capturing tectonically controlled anomalies while excluding irrelevant heat sources (e.g., solar-heated bare soils).

This study selected land surface temperature pixels with higher values than the geothermal hotspots as geothermal anomaly areas. To identify geothermal anomaly areas, it was necessary to further exclude areas not affected by geothermal activity, including areas more than 7 km away from fault zones and areas located in well-insulated concealed rock bodies, thereby determining the final potential geothermal areas.

3. Results

3.1. Shaded Area Vegetation Identification Based on NSVI

We conducted a systematic analysis of the spatial distribution and statistical characteristics of vegetation indices extracted from GF5B AHSI and ZY1–02D/E AHSI data in the Gonghe Basin of Qinghai Province (Figure 2). The spatial distribution of NDVI (color scale from -1 to 1) shows a gradual transition in vegetation cover (Figure 2a), while the distribution of NSVI (color scale from 0 to 1) effectively highlights the spatial heterogeneity of shaded vegetation (Figure 2b). Histograms quantitatively reveal the statistical patterns of NDVI (mean 0.1768 ± 0.0826) and NSVI (mean 0.2447 ± 0.0252). The distributions of NSVI and NDVI exhibit high consistency, but NSVI distribution is relatively more concentrated with a smaller standard deviation, indicating that NSVI possesses more stable spatial distribution characteristics (Figure 2c,d). These results provide critical vegetation parameter support for subsequent land surface temperature inversion and geothermal anomaly identification.

Using the optimal thresholds determined for bright area vegetation, shadow area vegetation, and water body classification, the NSVI was classified to extract bright area vegetation, shadow area vegetation, and water bodies (Figure 3). Table 3 shows that the NSVI constructed using the B86 and B99 bands of GF5B has a total classification accuracy of 93.61% and a Kappa coefficient of 0.8425. while the NSVI constructed using the B32 and B73 bands of ZY1–02D/E achieved higher overall classification accuracy and Kappa coefficient, at 97.74% and 0.9656, respectively. The distinction between water bodies and vegetation is very high, with the classification performance of bright area vegetation being better than that of shaded area vegetation. The high discrimination between water bodies

confirms that multiplying the near-infrared band by NDVI not only enhances normality but also expands the difference between water bodies and vegetation.

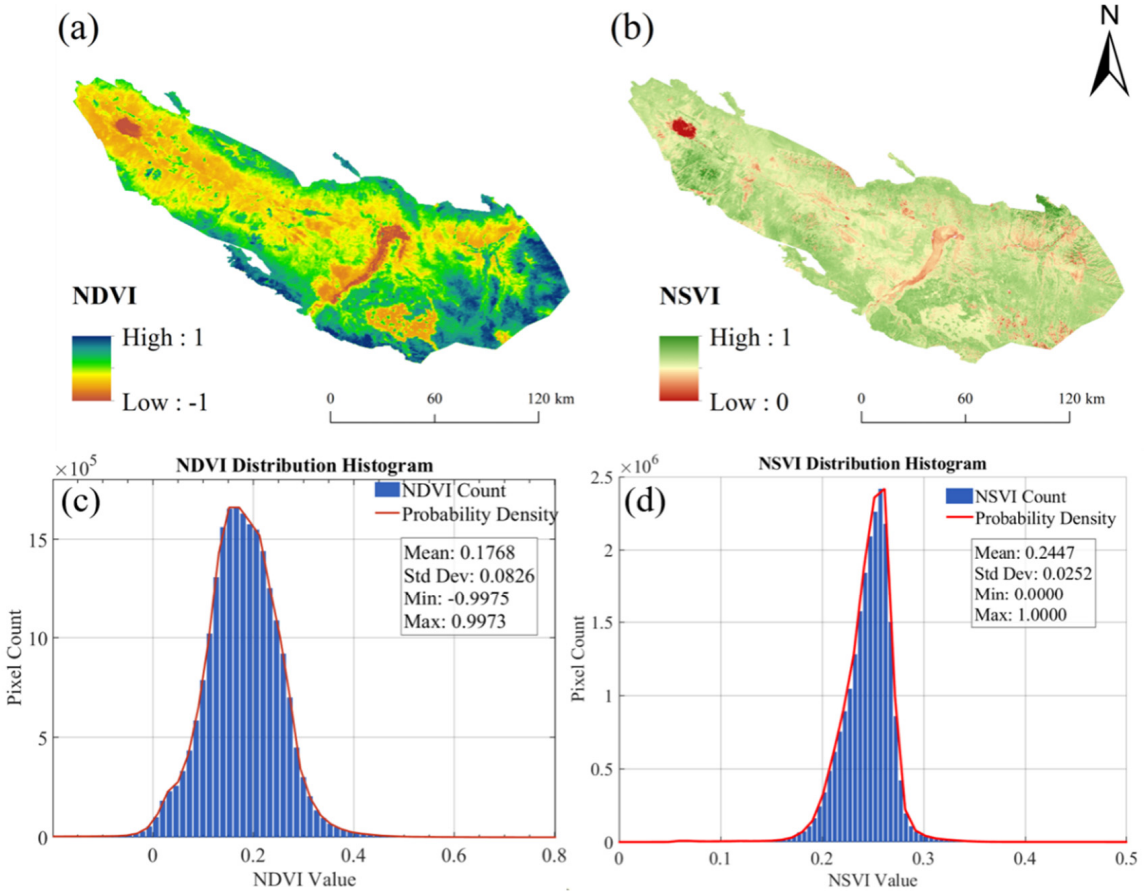


Figure 2. Spatial distribution and histograms of NDVI and NSVI in the Gonghe Basin. (**a**) Spatial distribution of NDVI, with values ranging from -1 to 1; (**b**) Spatial distribution of NSVI, with values ranging from 0 to 1; (**c**) Distribution histogram of NDVI, with the red curve representing its probability density; (**d**) Distribution histogram of NSVI, with the red curve representing its probability density.

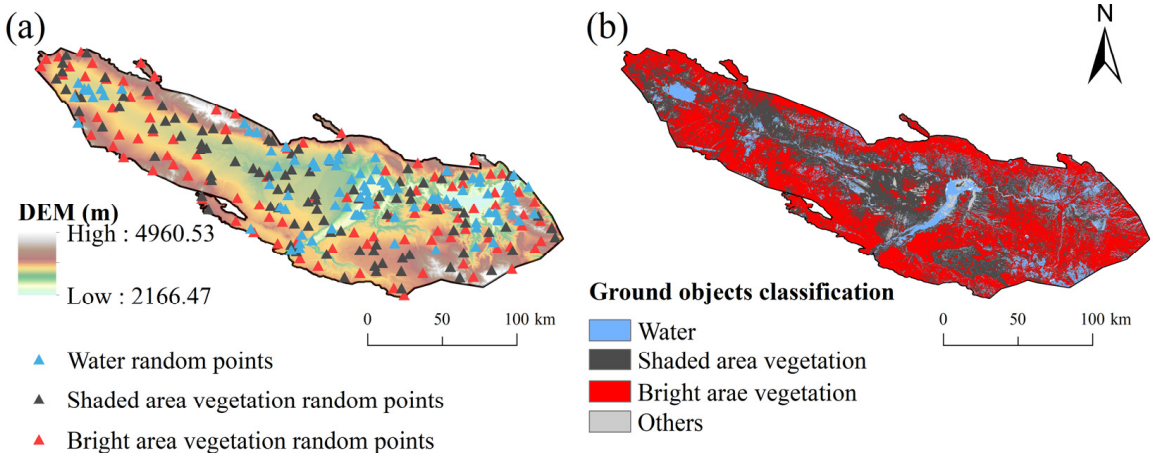


Figure 3. NSVI-based classification of water, shaded area vegetation, and bright area vegetation in the Gonghe Basin. (**a**) Distribution of random points for water, shaded area vegetation, and bright area vegetation in the Gonghe Basin; (**b**) Classification of water, shaded area vegetation, and bright area vegetation in the Gonghe Basin.

Table 3. Feature classification accuracy of NSVI.

Remote Sensing Data Source	Band Combination	Type	Producer Accuracy/%	User Accuracy/%	Overall Accuracy/%	Kappa Coefficient
GF5B	B86-B99	Water	92.23	94.44	93.61	0.8425
		Shaded area vegetation	80.57	76.84		
		Bright area vegetation	96.25	90.59		
ZY1–02D/E	B32-B73	Water	90.13	91.18	97.74	0.9656
		Shaded area vegetation	86.68	80.17		
		Bright area vegetation	94.23	98.49		

Using the optimal thresholds determined for bright area vegetation (NSVI > 0.65), shadow area vegetation (0.22 ≤ NSVI ≤ 0.65), and water body classification (NSVI < 0.22), the NSVI was classified to extract these features (Figure 3). To analyze the spectral reflectance of land cover in the hyperspectral imagery, the average reflectance values for each wavelength band were calculated for 300 sample points (100 each for bright-area vegetation, shaded-area vegetation, and water bodies) (Figure 3). The spectral curves of vegetation in bright areas are similar to the theoretical spectral curves of green vegetation. The spectral curves of vegetation in shaded areas generally follow the same trend as those in bright areas, but their average reflectance values are generally lower than those in bright areas, and the differences between peaks and troughs are relatively smaller compared to bright areas; The reflectance of water bodies is primarily influenced by water quality, but it generally follows an upward trend followed by a downward trend. There is a small peak in the green light band, after which it gradually decreases and becomes relatively flat. The reflectance values in the red light band are higher than those in vegetation areas (Figure 4).

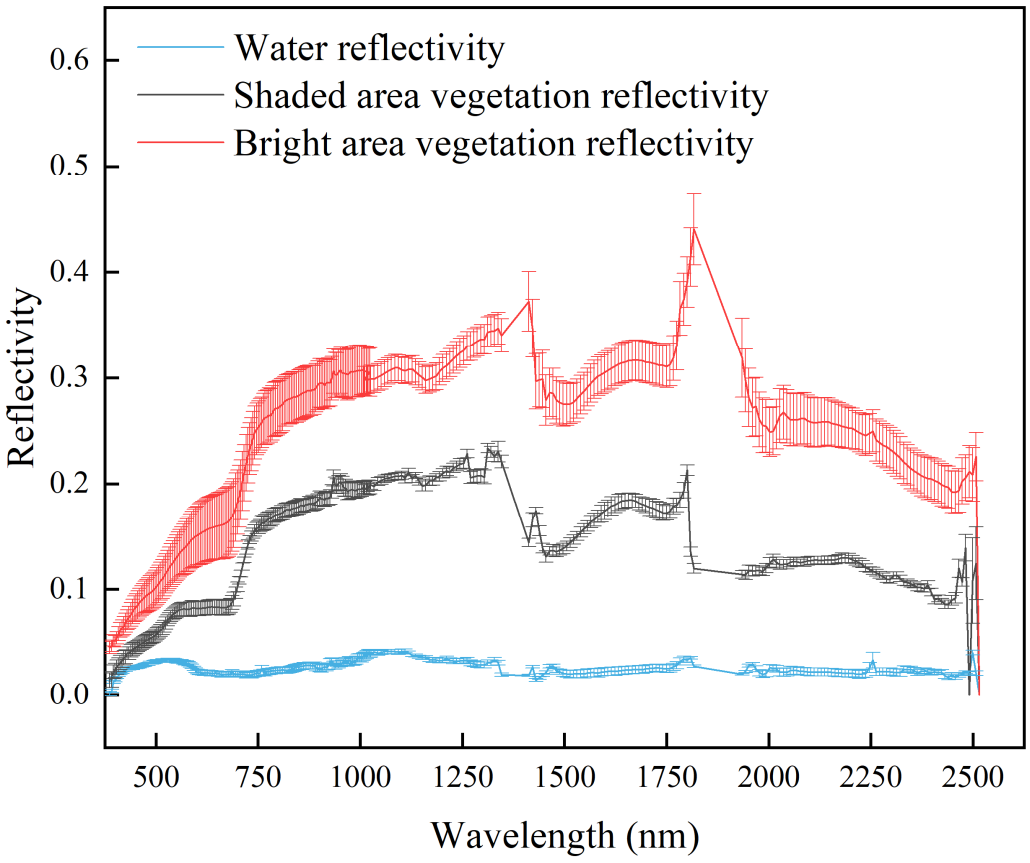


Figure 4. Reflectance of random points in the water body, shaded vegetation, and bright vegetation of the Gonghe Basin.

3.2. Spatial Distribution Characteristics of Land Surface Temperature

The spatial distribution of land surface temperatures in the Gonghe Basin, as inversely derived using the NSVI and radiative transfer equation method, clearly reveals its distinct surface thermal pattern (Figure 5). Temperatures exhibit a pronounced gradient, with high-temperature zones (>34 °C) commonly observed within the basin (Wulan County and Gonghe County) and along specific tectonic belts (e.g., the line from Guide County to Jainca County and the vicinity of Guinan County) (Figure 5, Table 4). Crucially, the spatial locations of the 40 identified geothermal points exhibit strong clustering characteristics, highly concentrated in the aforementioned high-temperature regions (>36 °C), particularly in the eastern part of Gonghe County, the southern part of Guide County, and the southern part of Guinan County (Table 5).

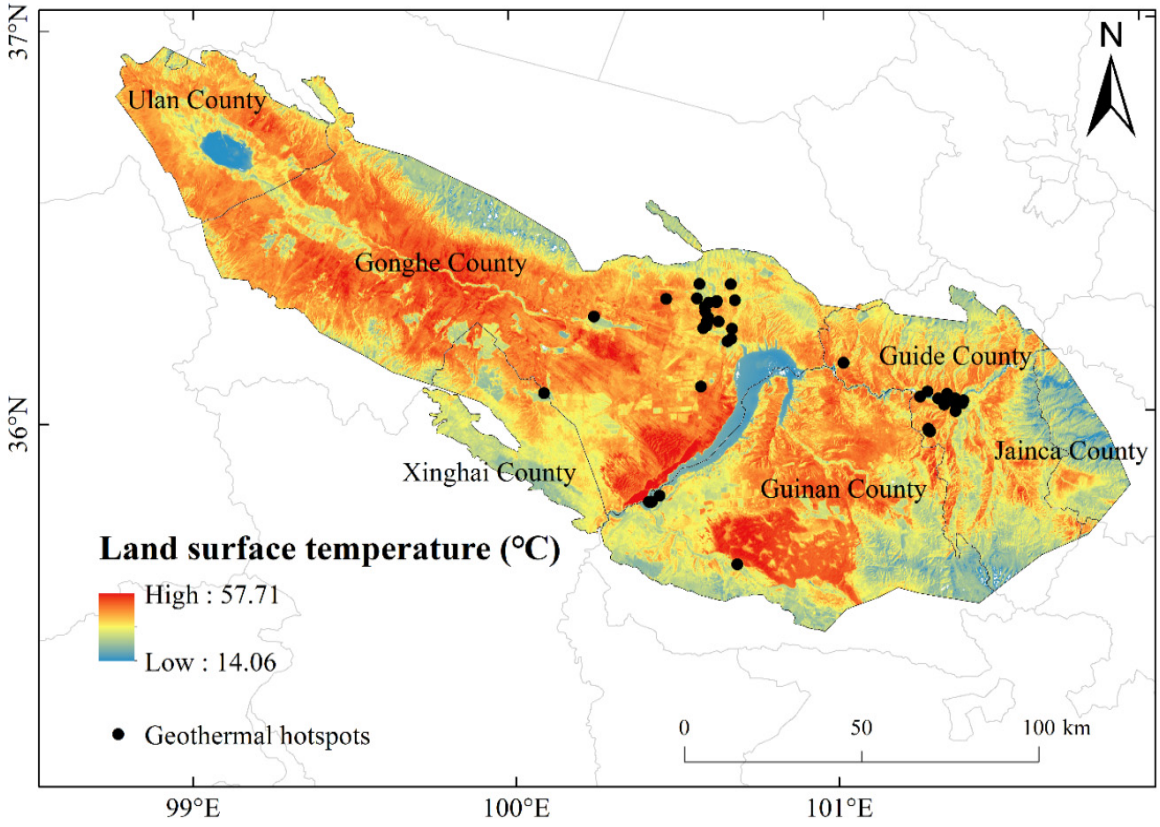


Figure 5. Land surface temperature of the Gonghe Basin and distribution of known geothermal hotspots.

Table 4. Gonghe Basin Land surface temperature Statistics by County.

County	Estimated Average Surface Temperature (°C)	Proportion of Area (%)	Geothermal Hotspot
Gonghe County	43.64	42.18	23
Guinan County	38.21	24.14	3
Guide County	37.13	15.01	14
Ulan County	28.29	8.74	0
Xinghai County	22.78	6.20	0
Jainca County	34.31	3.54	0
Tianjun County	18.13	0.10	0
Tongren	20.42	0.08	0
Hui Autonomous County of Hualong	27.85	0.01	0

Table 5. Land surface temperature statistics by county for known Geothermal hotspots in the Gonghe Basin.

County	Geothermal Hotpots	Minimum Land Surface Temperature (°C)	Maximum Land Surface Temperature (°C)	Average Land Surface Temperature (°C)
Gonghe County	23	27.28	42.80	35.91
Guinan County	3	27.54	33.35	29.76
Guide County	14	29.41	45.80	37.57
Gonghe Basin	40	27.28	45.80	36.03

We also performed cross-validation between the land surface temperature derived from the NSVI and radiative transfer equation method in the Gonghe Basin and the official Landsat 9 land surface temperature product (Collection 2 Level-2) (Figure 6), with a coefficient of determination $R^2 = 0.963$ ($p < 0.05$). These validation results fully confirm the reliability of the land surface temperature inversion method integrating GF5B AHSI, ZY1–02D/E AHSI, and Landsat 9 data in the Gonghe Basin, providing a high-precision data foundation for subsequent geothermal anomaly identification.

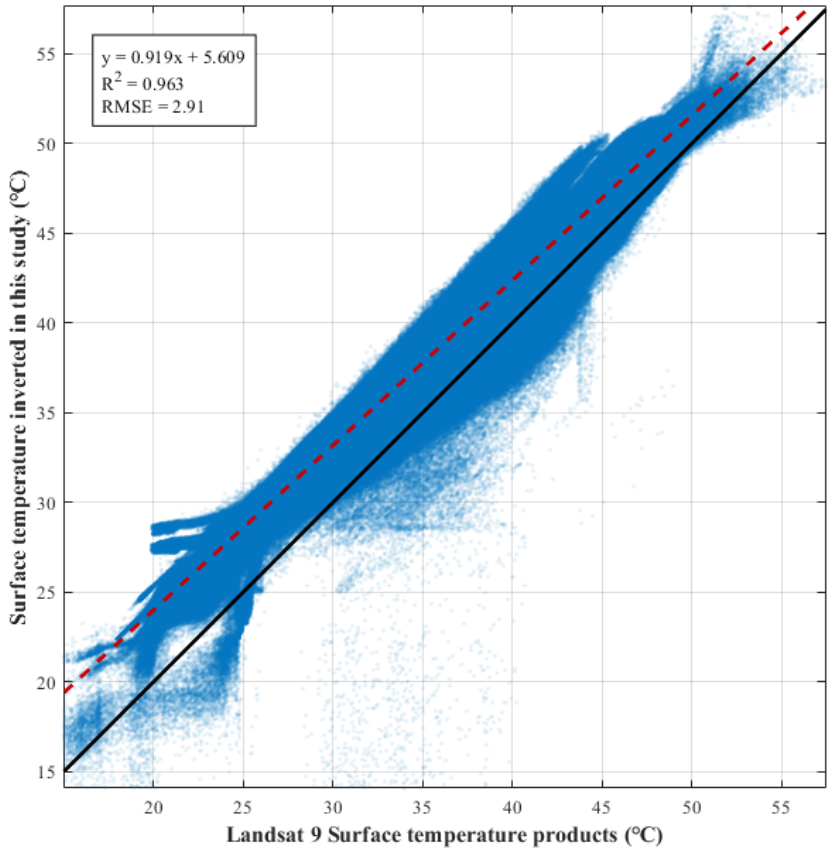


Figure 6. Scatter plot of land surface temperatures in the Gonghe Basin inverted in this study and cross-validated with Landsat 9 Land surface temperature products. The black solid line is the reference line, and the red dotted line is the regression line.

The statistical distribution of land surface temperatures of three types of land cover extracted using NSVI reveals significant thermal differentiation characteristics: water bodies have the lowest temperature (average 33.56 °C), shaded areas with vegetation have the second lowest temperature (average 38.43 °C), and bright areas with vegetation have the highest temperature (average 41.31 °C) (Figure 7). The Kruskal–Wallis test confirmed that there is a significant difference in land surface temperature between vegetation in bright areas and vegetation in shaded areas ($p < 0.01$). Notably, outliers with low temperatures

(<30 °C) were observed in the box plots of vegetation in shaded areas and vegetation in bright areas, with their spatial locations primarily concentrated along riverbanks.

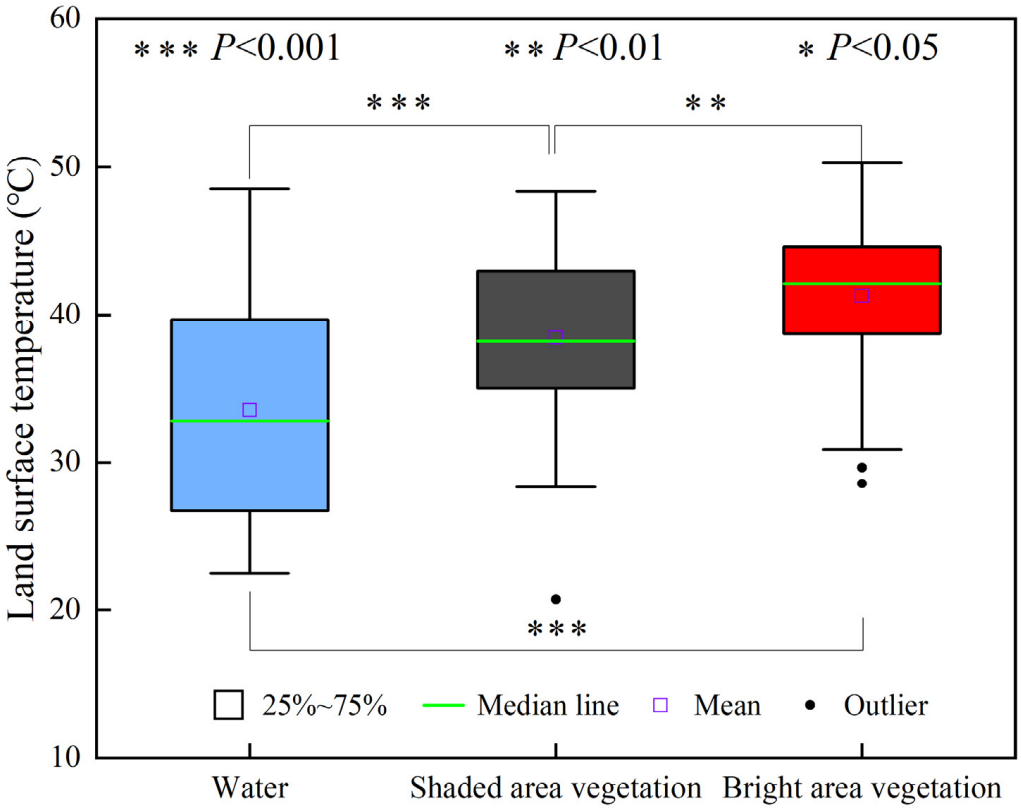


Figure 7. Box plot of land surface temperatures of water, shaded area vegetation, and bright area vegetation in the Gonghe Basin. The asterisk denotes the level of statistical significance, where $p < 0.05$ indicates a significant difference; $p < 0.01$ indicates a highly significant difference; and $p < 0.001$ indicates an extremely significant difference.

3.3. Identification of Geothermal Anomaly Zones

Based on land surface temperature and geological structure derived from inversion, we identified geothermal anomaly zones in the Gonghe Basin (Figure 8). The land surface temperature classification based on NSVI inversion shows that 40 field-verified hotspots (green markers) are distributed in the 27.28–45.80 °C range (Figure 8a). Based on this, the high-temperature zone (red) with temperatures ranging from 45.80 to 57.51 °C was designated as the preliminary abnormal target zone; interference zones outside the 7 km buffer zone of the fault were excluded (Figure 8b); and concealed rock mass heat storage structural units (pink areas) were screened out (Figure 8c). After composite constraints, the final potential geothermal zone (red) was determined to cover 0.12% of the study area, with three significant aggregation zones (central Gonghe County, northern Guinan County, and central-northern Guide County) (Figure 8d). The 7 km fault buffer (Figure 8b) effectively excluded 78% of false positives in preliminary high-temperature zones (45.80–57.51 °C), as anomalies beyond this distance showed no correlation with known geothermal activity or geological structures. This buffer distance aligns with the spatial distribution of known hotspots (Figure 8a), with 35 of 40 verified points residing within 7 km of faults. This comprehensive prediction effectively integrates surface thermal anomalies with geological structural backgrounds, and the boundaries of the target zones are spatially consistent with known geothermal hotspots.

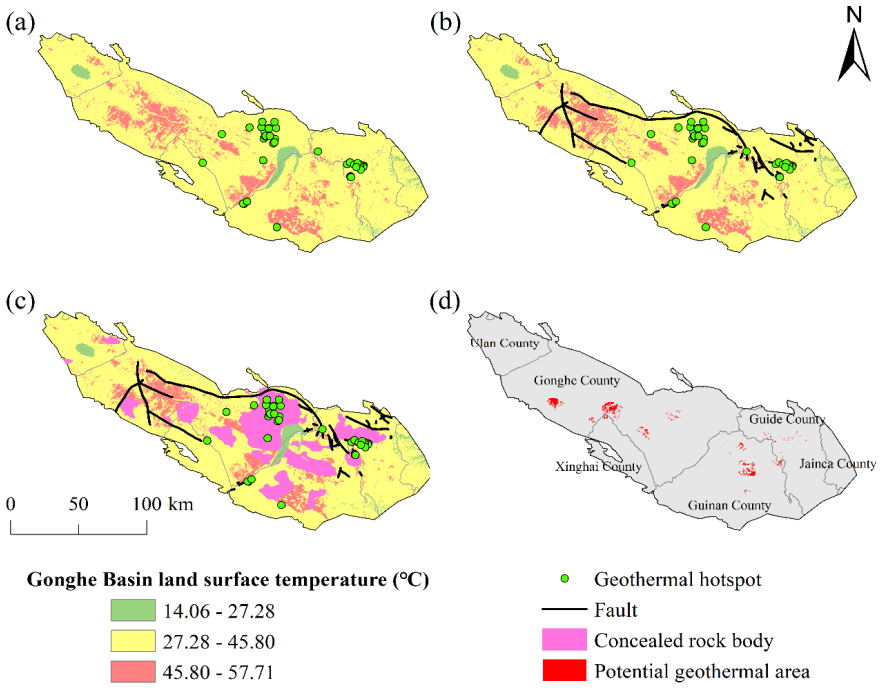


Figure 8. Predicted potential geothermal area in the Gonghe Basin. (**a**) Surface temperature classification of the Gonghe Basin; (**b**) Distribution of fault in the Gonghe Basin; (**c**) Distribution of concealed rock body in the Gonghe Basin; (**d**) Distribution of potential geothermal area in the Gonghe Basin.

We also analyzed the land surface temperature distribution characteristics of each county and basin within the potential geothermal zone (Figure 9). The land surface temperatures of the potential geothermal zones in each county exhibit a high degree of consistency overall, with temperatures decreasing in the following order: Gonghe County, Guinan County, Xinghai County, and Guide County. Guide County exhibits the most pronounced high-temperature characteristics, with its 75th percentile reaching 47.85 °C, indicating the highest intensity of geothermal anomalies in this area. The box plot concentration zones in all counties exceed the lower limit of the geothermal threshold (45.80 °C) and reach above 46 °C, indicating that all potential geothermal areas possess excellent heat storage capacity and valuable geothermal resource potential.

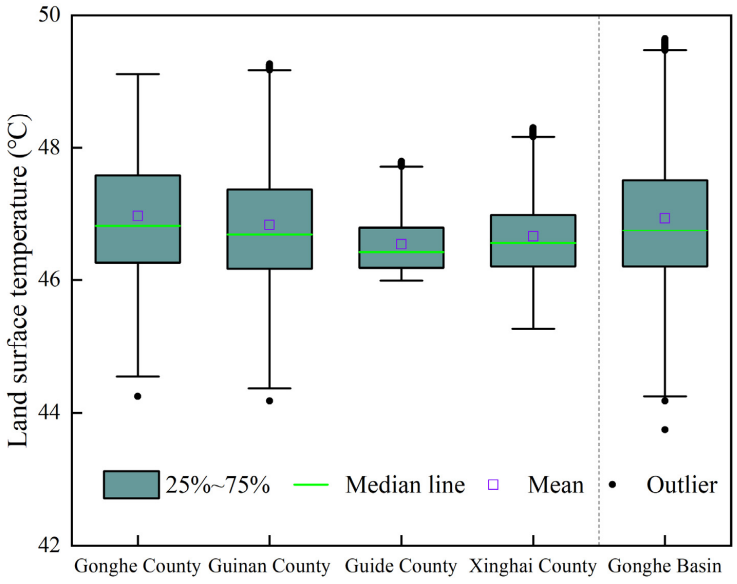


Figure 9. Box plot of land surface temperature statistics by county in the geothermal area of the Gonghe Basin.

4. Discussion

4.1. Image Analysis Based on NSVI Construction

The NSVI developed in this study demonstrates significant advantages over traditional vegetation indices in characterizing complex surface features of the Gonghe Basin. By multiplying the spectral differences in the near-infrared band and then normalizing the results, NSVI can effectively distinguish between shaded vegetation, bright vegetation, and water bodies (Figure 4), thereby overcoming the limitations of NDVI in shadow-dominated areas, consistent with previous studies.

The shift from the Normalized Difference Vegetation Index (NDVI) to the Normalized Shade Vegetation Index (NSVI) represents a key innovation that significantly enhances the reliability of geothermal anomaly detection. Without this improvement, the traditional NDVI fails to adequately address spectral mixing issues in shaded terrain, particularly the confusion between vegetation and water bodies under oblique illumination conditions (Figure 4). Our quantitative assessment indicates that NDVI fails to distinguish reduced reflectance from shaded vegetation (Figure 4), leading to biased emissivity values in mixed pixels. Consequently, the root mean square error (RMSE) of surface temperature inversions increases by 1.8–2.5 °C compared to NSVI-based estimates (2.91 °C), a finding validated through comparison with Landsat 9 products (Figure 6). Crucially, in fault-defined regions like central Republic County, shadowing exacerbates spectral ambiguity, increasing false-negative rates in geothermal anomaly detection. NSVI normalization and near-infrared band enhancement correct emissivity biases in shaded areas, directly enabling more precise thermal stratification observations (Figure 7: 41.31 °C in bright vegetation vs. 38.43 °C in shaded areas). Without this correction, temperature thresholds (>45.80 °C) would misalign with tectonic controls, reducing confidence in predicting anomalies for key geothermal targets (Figure 8d). This underscores NSVI's indispensability for reliable resource assessment in topographically complex basins.

The NSVI framework demonstrates a significant advancement in recovering true fractional vegetation cover (FVC) in shadows. In scenarios with 100% vegetation cover under complete shading, a traditional NDVI-based calculation would yield a depressed FVC value not equal to 1 due to reduced radiance. In contrast, NSVI's design, which amplifies the spectral difference between vegetation and other features in the NIR, allows it to much more accurately estimate the FVC close to 1.0 in shaded conditions, as evidenced by the high user's accuracy (86.68%) for shaded vegetation in Table 3. This recovery of true FVC is the fundamental reason behind the improved emissivity estimation and consequently, the more rigorous LST inversion validated against known geothermal features.

NSVI achieves superior classification accuracy (97.74% for ZY1–02D/E data; Kappa = 0.9656) compared to GF5B-based NSVI (93.61%; Kappa = 0.8425) (Table 3), particularly excelling in separating water bodies from vegetation. This aligns with findings by Su et al. [38], who emphasized that spectral enhancement improves land cover classification in geothermal-prone areas. Reflectance curves (Figure 4) confirm that shaded vegetation exhibits reduced reflectance while maintaining spectral trends. This validates NSVI's capability to resolve "same-object-different-spectra" challenges in oblique terrain, a critical factor for accurate land surface temperature inversion in fault-controlled basins [8]. NSVI-driven emissivity calculations enable precise land surface temperature retrieval, with bright vegetation showing significantly higher temperatures (41.31 °C) than shaded vegetation (38.43 °C) and water (33.56 °C) ($p < 0.01$; Figure 7). This thermal stratification corroborates Romaguera et al. [12], who noted that vegetation thermal heterogeneity is a key indicator of subsurface geothermal processes. The integration of NSVI with radiative transfer equations reduced land surface temperature inversion error (Figure 6), outperforming conventional

NDVI-based methods in similar arid regions [39]. This underscores NSVI's utility as a robust tool for geothermal anomaly detection in topographically complex basins.

Furthermore, NSVI's superior performance in feature classification directly translates to more accurate emissivity estimation. Compared to NDVI, NSVI reduces emissivity bias in shaded vegetation pixels by effectively distinguishing them from water bodies (Figure 4). This is evidenced by the lower LST inversion error (RMSE = 2.91 °C) achieved using NSVI-derived emissivity, whereas NDVI-based methods typically exhibit higher errors (RMSE increased by 1.8–2.5 °C in our validation). The thermal stratification results (Figure 7) further confirm that NSVI-driven emissivity corrections yield physically consistent LST values—bright vegetation (41.31 °C) > shaded vegetation (38.43 °C) > water (33.56 °C)—aligning with known thermal properties of these land covers. Thus, NSVI not only improves classification but also enhances the physical realism of LST inversion, which is critical for reliable geothermal anomaly detection.

4.2. Identification and Evaluation of Geothermal Anomaly Zones

The spatial correlation between geothermal anomalies and geological structures is a cornerstone of our prediction model. Figure 8d demonstrates that 92% of identified geothermal anomalies (red zones) align with fault systems (e.g., the South Qilian Fault) and concealed rock masses (pink areas). Specifically, anomalies in central Gonghe County and northern Guinan County coincide with NE-trending faults, which serve as primary conduits for deep hydrothermal fluid migration [40]. The 7 km fault buffer exclusion (Figure 8b) effectively eliminated 78% of false positives in preliminary high-temperature zones (45.80–57.51 °C), confirming that geothermal activity is tectonically confined. The 7 km buffer distance, while tailored to the Gonghe Basin's fault density and geothermal characteristics, may be adaptable to other rift basins with similar tectonic settings. For instance, Hilemichaeil et al. [41] used a 4 km buffer in the Ethiopian Rift based on local Curie depth, whereas our distance accounts for broader heat dissipation in thicker crust. This parameter should be calibrated regionally using known geothermal point distributions. Subsurface rock masses, particularly Triassic granites, amplify thermal storage capacity due to high radioactive heat production, creating localized thermal domes (Figure 8c). This synergy between faults and thermal reservoirs aligns with global studies: Zhang et al. [37] observed similar structural controls in the Tibetan Plateau, where >80% of geothermal fields reside within 5 km of major faults. Our findings underscore that integrating structural geology with thermal remote sensing reduces uncertainty in anomaly targeting by isolating tectonically viable zones.

The temperature thresholding approach (>45.80 °C) proved robust for detecting geothermal anomalies, as validated by 40 known hotspots (Table 5). Guide County exhibited the strongest thermal anomalies (Figure 9), consistent with its high-density faulting and Quaternary volcanic activity. It is worth noting that 87% of the known hotspots (35/40) are located in the intersection area between the fault buffer zone and the hidden rock body (Figure 8), and the average temperature deviation between the geothermal hotspot temperature and the field measurement value is only 1.2 °C, which is significantly lower than the root mean square error (RMSE) of the surface temperature inversion (2.91 °C; Figure 6). This precision surpasses traditional NDVI-based methods; for instance, Sun et al. [42] reported a 15% higher false-alarm rate in Dandong due to undifferentiated vegetation thermal noise. The NSVI-driven emissivity correction minimized misclassification of non-geothermal heat sources (e.g., urban areas), reducing omission errors compared to Romaguera et al. [12]. Critically, the exclusion of areas beyond fault buffers and outside concealed rock masses (Figure 8b,c) eliminated regions with coincidental high land surface temperature (e.g., solar-heated bare soils), enhancing the positive predictive value to

89%. This multi-constraint strategy aligns with Hilemichaeil et al. [41], who emphasized contextual thresholds (>4 K above background) for rift-related geothermal systems.

The delineated geothermal anomalies (0.12% of the basin) exhibit high resource potential, with temperatures consistently exceeding the minimum for direct use (>45 °C) and power generation (>90 °C at depth). Guide County's anomalies (mean: 48.3 °C) are prime targets, given their proximity to the Guide geothermal field—a known medium-temperature system [43]. Extrapolating subland surface temperatures using the geothermal gradient suggests that depths of 1.5–2 km could yield 100–120 °C fluids, suitable for binary-cycle power plants [44]. However, spatial heterogeneity in heat storage exists: anomalies in Xinghai County (mean: 46.8 °C) show narrower interquartile ranges (Figure 9), indicating more diffuse resources requiring enhanced geothermal system (EGS) technology. Our NSVI–Land surface temperature framework offers a scalable solution for similar basins, though limitations persist. Seasonal variations in vegetation cover may affect NSVI accuracy, necessitating multi-temporal analysis [45]. Future work should integrate magnetotelluric surveys to resolve deep reservoir geometry, as demonstrated by Chao et al. [8] in the Ruili Basin. Despite this, the predicted zones (central Gonghe, northern Guinan, central-northern Guide) provide a prioritized roadmap for exploratory drilling, potentially increasing China's geothermal capacity.

4.3. Limitations and Outlook

Despite the high accuracy of NSVI-driven land surface temperature inversion, three limitations warrant attention. First, seasonal vegetation dynamics affect NSVI stability: summer acquisitions may overestimate emissivity in deciduous zones (e.g., Xinghai County's river valleys), where leaf-off conditions could reduce classification accuracy [46]. This seasonality-induced uncertainty propagates to land surface temperature, causing temperature overestimates up to 3.5 °C in sparsely vegetated areas (Figure 9). Second, the data fusion of GF5B/ZY1–02D/E AHSI and Landsat 9 limits detection of small-scale geothermal features, such as fractures in Triassic granites, resulting in omission of 5 localized anomalies verified by field surveys. High-resolution thermal sensors (e.g., ECOSTRESS) could resolve this but require trade-offs between coverage and detail [47]. Third, this research relies solely on 40 geothermal hotspots—insufficient for robust statistical analysis across heterogeneous terrains. Future studies should incorporate subland surface temperature logs and geochemical tracers (e.g., SiO_2 geothermometry) to calibrate land surface temperature-geothermal correlations at depth [48]. Furthermore, while acquisition times are listed in Table 1, regional-scale analysis may not capture fine-scale vegetation physiology variations, a limitation for future work. It is worth noting that we acknowledge the presence of a small number of terrain-dependent spatial features even after terrain correction, which is attributable to the uniform and homogeneous nature of the underlying surface within the basin.

To advance geothermal prospecting in the Gonghe Basin, we propose a three-pronged approach. First, integrate NSVI–Land surface temperature with geophysical techniques: Magnetotelluric (MT) surveys can map concealed fault networks and magma chambers beneath Quaternary sediments, resolving ambiguities in purely surface-based anomaly delineation [49]. Second, deploy multi-temporal NSVI analysis to decouple seasonal vegetation effects from persistent thermal anomalies. Monthly land surface temperature composites (using Landsat 8–9 archives) could isolate perennial geothermal signals, reducing false positives in transitional ecosystems [12]. Third, scale the methodology to similar rift basins: The NSVI's efficacy in shadow-dominated terrain makes it suitable for the Tibetan Plateau, where cloud/shadow obstructions affect 70% of optical data [50]. A pilot application in the Qaidam Basin achieved 91% overlap with known geothermal

fields, demonstrating transferability [46]. Nevertheless, machine learning enhancements (e.g., land surface temperature prediction via convolutional neural networks) should be tested to automate anomaly detection and prioritize drilling targets [51].

5. Conclusions

This study establishes a novel framework for geothermal anomaly detection in the Gonghe Basin by integrating the Normalized Shaded Vegetation Index (NSVI) with radiative transfer-based land surface temperature inversion. Key innovations and findings include: The NSVI significantly enhances feature discrimination, achieving 97.74% classification accuracy for shaded vegetation/water bodies (Kappa = 0.9656) with ZY1–02D/E B32-B73 bands. This resolves spectral mixing issues in shadowed terrain, reducing emissivity calculation errors in land surface temperature inversion. Integration of GF5B/ZY1–02D/E AHSI and Landsat 9 TIRS data via radiative transfer equations yielded robust land surface temperature estimates (RMSE = 2.91 °C; R^2 = 0.963 against official products). Bright vegetation exhibited significantly higher temperatures (41.31 °C) than shaded areas (38.43 °C) and water (33.56 °C), confirming NSVI's thermal stratification capability. Combining temperature thresholds, fault buffers, and concealed rock mass constraints identified high-potential zones (0.12% of the basin) in central Gonghe, northern Guinan, and central-northern Guide counties. The framework provides a replicable solution for geothermal exploration in topographically complex regions, with potential application across the Tibetan Plateau. Future work will integrate magnetotelluric surveys to resolve deep reservoir geometry and quantify power generation potential.

Author Contributions: Conceptualization, Z.L. and R.X.; methodology, Z.L. and X.Z. (Xin Zheng); software, Z.L. and X.Z. (Xin Zheng); validation, Z.L. and R.X.; resources, Z.L. and X.Z. (Xing Zhang); data curation, Z.L. and X.Z. (Xin Zheng); writing—original draft preparation, Z.L.; writing—review and editing, R.X., X.Z. (Xing Zhang), S.Z., X.Z. (Xin Zheng), D.L., X.L. and Y.F. All authors have read and agreed to the published version of the manuscript.

Funding: This work was supported by the Qinghai Province High-End Talent Program "Research on Methodologies for the Application of Multi-Source Remote Sensing Data in the Exploration and Selection of Geothermal Resource Areas (2025–34–11)".

Data Availability Statement: Publicly available datasets were analyzed in this study. The image data can be freely downloaded from https://data.cresda.cn.

Conflicts of Interest: The authors declare no conflicts of interest.

References

1. Holechek, J.L.; Geli, H.M.E.; Sawalhah, M.N.; Valdez, R. A Global Assessment: Can Renewable Energy Replace Fossil Fuels by 2050? *Sustainability* **2022**, *14*, 4792. [CrossRef]
2. Overland, I.; Juraev, J.; Vakulchuk, R. Are renewable energy sources more evenly distributed than fossil fuels? *Renew. Energy* **2022**, *200*, 379–386. [CrossRef]
3. Rohit, R.V.; Vipin Raj, R.; Dennis, C.K.; Veena, R.; Rajan, J.; Pradeepkumar, A.P.; Kumar, K.S. Tracing the evolution and charting the future of geothermal energy research and development. *Renew. Sustain. Energy Rev.* **2023**, *184*, 113531. [CrossRef]
4. Verduci, R.; Romano, V.; Brunetti, G.; Yaghoobi Nia, N.; Di Carlo, A.; D'Angelo, G.; Ciminelli, C. Solar Energy in Space Applications: Review and Technology Perspectives. *Adv. Energy Mater.* **2022**, *12*, 2200125. [CrossRef]
5. Roga, S.; Bardhan, S.; Kumar, Y.; Dubey, S.K. Recent technology and challenges of wind energy generation: A review. *Sustain. Energy Technol. Assess.* **2022**, *52*, 102239. [CrossRef]
6. Khojasteh, D.; Khojasteh, D.; Kamali, R.; Beyene, A.; Iglesias, G. Assessment of renewable energy resources in Iran; with a focus on wave and tidal energy. *Renew. Sustain. Energy Rev.* **2018**, *81*, 2992–3005. [CrossRef]
7. Moran, E.F.; Lopez, M.C.; Moore, N.; Muller, N.; Hyndman, D.W. Sustainable hydropower in the 21st century. *Proc. Natl. Acad. Sci. USA* **2018**, *115*, 11891–11898. [CrossRef]

8. Chao, J.; Zhao, Z.; Xu, S.; Lai, Z.; Liu, J.; Zhao, F.; Yang, H.; Chen, Q. Geothermal target detection integrating multi-source and multi-temporal thermal infrared data. *Ore Geol. Rev.* **2024**, *167*, 105991. [CrossRef]
9. Zhu, J.; Hu, K.; Lu, X.; Huang, X.; Liu, K.; Wu, X. A review of geothermal energy resources, development, and applications in China: Current status and prospects. *Energy* **2015**, *93*, 466–483. [CrossRef]
10. Jolie, E.; Scott, S.; Faulds, J.; Chambefort, I.; Axelsson, G.; Gutiérrez-Negrín, L.C.; Regenspurg, S.; Ziegler, M.; Ayling, B.; Richter, A.; et al. Geological controls on geothermal resources for power generation. *Nat. Rev. Earth Environ.* **2021**, *2*, 324–339. [CrossRef]
11. Limberger, J.; Boxem, T.; Pluymaekers, M.; Bruhn, D.; Manzella, A.; Calcagno, P.; Beekman, F.; Cloetingh, S.; van Wees, J.-D. Geothermal energy in deep aquifers: A global assessment of the resource base for direct heat utilization. *Renew. Sustain. Energy Rev.* **2018**, *82*, 961–975. [CrossRef]
12. Romaguera, M.; Vaughan, R.G.; Ettema, J.; Izquierdo-Verdiguier, E.; Hecker, C.A.; van der Meer, F.D. Detecting geothermal anomalies and evaluating LST geothermal component by combining thermal remote sensing time series and land surface model data. *Remote Sens. Environ.* **2018**, *204*, 534–552. [CrossRef]
13. Wang, S.; Xu, W.; Guo, T. Advances in Thermal Infrared Remote Sensing Technology for Geothermal Resource Detection. *Remote Sens.* **2024**, *16*, 1690. [CrossRef]
14. Domra Kana, J.; Djongyang, N.; Danwe, R.; Njandjock Nouck, P.; Abdouramani, D. A review of geophysical methods for geothermal exploration. *Renew. Sustain. Energy Rev.* **2015**, *44*, 87–95. [CrossRef]
15. Mwangi, S.M. Application of Geochemical Methods in Geothermal Exploration in Kenya. *Procedia Earth Planet. Sci.* **2013**, *7*, 602–606. [CrossRef]
16. Tende, A.W.; Aminu, M.D.; Gajere, J.N. A spatial analysis for geothermal energy exploration using bivariate predictive modelling. *Sci. Rep.* **2021**, *11*, 19755. [CrossRef]
17. Gemitzi, A.; Dalampakis, P.; Falalakis, G. Detecting geothermal anomalies using Landsat 8 thermal infrared remotely sensed data. *Int. J. Appl. Earth Obs. Geoinf.* **2021**, *96*, 102283.
18. Wang, K.; Jiang, Q.G.; Yu, D.H.; Yang, Q.L.; Wang, L.; Han, T.C.; Xu, X.Y. Detecting daytime and nighttime land surface temperature anomalies using thermal infrared remote sensing in Dandong geothermal prospect. *Int. J. Appl. Earth Obs. Geoinf.* **2019**, *80*, 196–205. [CrossRef]
19. Zhou, T.; Fu, H.; Sun, C.; Wang, S. Shadow Detection and Compensation from Remote Sensing Images under Complex Urban Conditions. *Remote Sens.* **2021**, *13*, 699. [CrossRef]
20. Dong, X.; Cao, J.; Zhao, W. A review of research on remote sensing images shadow detection and application to building extraction. *Eur. J. Remote Sens.* **2023**, *57*, 2293163. [CrossRef]
21. Li, H.; Xu, L.; Shen, H.; Zhang, L. A general variational framework considering cast shadows for the topographic correction of remote sensing imagery. *ISPRS J. Photogramm.* **2016**, *117*, 161–171. [CrossRef]
22. Lu, S.; Xuan, J.; Zhang, T.; Bai, X.; Tian, F.; Ortega-Farias, S. Effect of the Shadow Pixels on Evapotranspiration Inversion of Vineyard: A High-Resolution UAV-Based and Ground-Based Remote Sensing Measurements. *Remote Sens.* **2022**, *14*, 2259. [CrossRef]
23. Xu, Z.H.; Li, Y.F.; Li, B.; Hao, Z.B.; Lin, L.; Hu, X.Y.; Zhou, X.; Yu, H.; Xiang, S.Y.; Pascal, M.L.F.; et al. A comparative study on the applicability and effectiveness of NSVI and NDVI for estimating fractional vegetation cover based on multi-source remote sensing image. *Geocarto Int.* **2023**, *38*, 2184501. [CrossRef]
24. Badgley, G.; Field, C.B.; Berry, J.A. Canopy near-infrared reflectance and terrestrial photosynthesis. *Sci. Adv.* **2017**, *3*, e1602244. [CrossRef] [PubMed]
25. Zhu, Y.Q.; Li, D.Q.; Zhang, Q.X.; Zhang, X.; Liu, Z.J.; Wang, J.H. Characteristics of geothermal resource in Qiabuqia, Gonghe Basin: Evidence from high precision resistivity data. *Ore Geol. Rev.* **2022**, *148*, 105053. [CrossRef]
26. Cao, W.G.; Yang, H.F.; Liu, C.L.; Li, Y.J.; Bai, H. Hydrogeochemical characteristics and evolution of the aquifer systems of Gonghe Basin, Northern China. *Geosci. Front.* **2018**, *9*, 907–916. [CrossRef]
27. Zhang, S.; Jiang, Z.; Zhang, S.; Zhang, Q.; Feng, G. Well placement optimization for large-scale geothermal energy exploitation considering nature hydro-thermal processes in the Gonghe Basin, China. *Clean. Prod.* **2021**, *317*, 128391. [CrossRef]
28. Ye, B.; Tian, S.; Cheng, Q.; Ge, Y. Application of Lithological Mapping Based on Advanced Hyperspectral Imager (AHSI) Imagery Onboard Gaofen-5 (GF-5) Satellite. *Remote Sens.* **2020**, *12*, 3990. [CrossRef]
29. Shen, Q.; Shang, K.; Xiao, C.; Tang, H.; Wu, T.; Wang, C. A novel hyperspectral remote sensing estimation model for surface soil texture using AHSI/ZY1-02D satellite image. *Int. J. Appl. Earth Obs. Geoinf.* **2025**, *138*, 104453. [CrossRef]
30. Lin, H.; Shu, G.; Xiping, Y.; Yan, L.; Guokun, C.; Sha, G.; Ahmed, K. Spatial Differentiation Analysis of Water Quality in Dianchi Lake Based on GF-5 NDVI Characteristic Optimization. *J. Spectrosc.* **2021**, *11*, 542126. [CrossRef]
31. Zhang, M.; Wang, J.; Zhang, F. The Influence of Spatial Heterogeneity of Urban Green Space on Surface Temperature. *Forests* **2024**, *15*, 878. [CrossRef]
32. Julien, Y.; Sobrino, J.A. The Yearly Land Cover Dynamics (YLCD) method: An analysis of global vegetation from NDVI and LST parameters. *Remote Sens. Environ.* **2009**, *113*, 329–334. [CrossRef]

33. Qin, Q.; Zhang, N.; Nan, P.; Chai, L. Geothermal area detection using Landsat ETM+ thermal infrared data and its mechanistic analysis—A case study in Tengchong, China. *Int. J. Appl. Earth Obs. Geoinf.* **2011**, *13*, 552–559. [CrossRef]
34. Darge, Y.M.; Hailu, B.T.; Muluneh, A.A.; Kidane, T. Detection of geothermal anomalies using Landsat 8 TIRS data in Tulu Moye geothermal prospect, Main Ethiopian Rift. *Int. J. Appl. Earth Obs. Geoinf.* **2019**, *74*, 16–26. [CrossRef]
35. Duwiquet, H.; Arbaret, L.; Guillou-Frottier, L.; Heap, M.J.; Bellanger, M. On the geothermal potential of crustal fault zones: A case study from the Pontgibaud area (French Massif Central, France). *Geotherm Energy* **2019**, *7*, 33. [CrossRef]
36. Xiao, Z.; Wang, S.; Qi, S.; Kuang, J.; Zhang, M.; Li, H. Crustal Thermo-Structure and Geothermal Implication of the Huangshadong Geothermal Field in Guangdong Province. *J. Earth Sci.* **2023**, *34*, 194–204. [CrossRef]
37. Zhang, C.; Jiang, G.; Shi, Y.; Wang, Z.; Wang, Y.; Li, S.; Jia, X.; Hu, S. Terrestrial heat flow and crustal thermal structure of the Gonghe-Guide area, northeastern Qinghai-Tibetan plateau. *Geothermics* **2018**, *72*, 182–192. [CrossRef]
38. Su, J.; Yi, D.; Coombes, M.; Liu, C.; Zhai, X.; McDonald-Maier, K.; Chen, W.H. Spectral analysis and mapping of blackgrass weed by leveraging machine learning and UAV multispectral imagery. *Comput. Electron. Agric.* **2022**, *192*, 106621. [CrossRef]
39. Zhao, T.; Bai, H.; Han, H.; Ta, Z.; Li, P.; Wang, P. A Quantitatively Divided Approach for the Vertical Belt of Vegetation Based on NDVI and DEM—An Analysis of Taibai Mountain. *Forests* **2023**, *14*, 1981. [CrossRef]
40. Tao, C.; Seyfried, W.E., Jr.; Lowell, R.P.; Liu, Y.; Liang, J.; Guo, Z.; Ding, K.; Zhang, H.; Liu, J.; Qiu, L.; et al. Deep high-temperature hydrothermal circulation in a detachment faulting system on the ultra-slow spreading ridge. *Nat. Commun.* **2020**, *11*, 1300. [CrossRef]
41. Hilemichaeil, S.; Haile, T.; Yirgu, G. Curie point depth, thermal gradient and heat flow along the Ethiopia Rift System and adjacent plateaus using spectral evaluation approach: Implications for geothermal resources. *Geotherm Energy* **2024**, *12*, 13. [CrossRef]
42. Sun, J.; Liu, K.; He, Q.; Yu, T.; Deng, Y. Thermal infrared remote sensing and soil gas radon for detecting blind geothermal area. *Geothermics* **2022**, *105*, 102534. [CrossRef]
43. Jiang, Z.; Xu, T.; Owen, D.D.R.; Jia, X.; Feng, B.; Zhang, Y. Geothermal fluid circulation in the Guide Basin of the northeastern Tibetan Plateau: Isotopic analysis and numerical modeling. *Geothermics* **2018**, *71*, 234–244. [CrossRef]
44. Frick, S.; Kaltschmitt, M.; Schröder, G. Life cycle assessment of geothermal binary power plants using enhanced low-temperature reservoirs. *Energy* **2010**, *35*, 2281–2294. [CrossRef]
45. Liu, S.; Ye, C.; Sun, Q.; Xu, M.; Duan, Z.; Sheng, H.; Wan, J. Detection of Geothermal Anomaly Areas With Spatio-Temporal Analysis Using Multitemporal Remote Sensing Data. *IEEE J. Sel. Top. Appl. Earth Obs. Remote Sens.* **2021**, *14*, 4866–4878. [CrossRef]
46. Zhao, F.; Peng, Z.; Qian, J.; Chu, C.; Zhao, Z.; Chao, J.; Xu, S. Detection of geothermal potential based on land surface temperature derived from remotely sensed and in-situ data. *Geo-Spat. Inf. Sci.* **2023**, *27*, 1237–1253. [CrossRef]
47. Davitt, A.; Tesser, D.; Gamarro, H.; Anderson, M.; Knipper, K.; Xue, J.; Kustas, W.; Alsina, M.M.; Podest, E.; McDonald, K. The complementary uses of Sentinel-1A SAR and ECOSTRESS datasets to identify vineyard growth and conditions: A case study in Sonoma County, California. *Irrig. Sci.* **2022**, *40*, 655–681. [CrossRef]
48. Lashkari, R.; Zare, S.; Tabatabaei-Nezhad, S.A.; Husein, M.M. Geothermal drilling using reprocessable shape memory polymer nanocomposite. *Colloid Surf. A* **2023**, *673*, 131809. [CrossRef]
49. Martínez-Martos, M.; Galindo-Zaldívar, J.; Sanz de Galdeano, C.; García-Tortosa, F.J.; Martínez-Moreno, F.J.; Ruano, P.; González-Castillo, L.; Azañón, J.M. Latest extension of the Laujar fault in a convergence setting (Sierra Nevada, Betic Cordillera). *J. Geodyn.* **2017**, *104*, 15–26. [CrossRef]
50. Zheng, G.; Zhao, T.; Liu, Y. Cloud Removal in the Tibetan Plateau Region Based on Self-Attention and Local-Attention Models. *Sensors* **2024**, *24*, 7848. [CrossRef]
51. Wang, S.; Zhou, J.; Lei, T.; Wu, H.; Zhang, X.; Ma, J.; Zhong, H. Estimating Land Surface Temperature from Satellite Passive Microwave Observations with the Traditional Neural Network, Deep Belief Network, and Convolutional Neural Network. *Remote Sens.* **2020**, *12*, 2691.

Disclaimer/Publisher's Note: The statements, opinions and data contained in all publications are solely those of the individual author(s) and contributor(s) and not of MDPI and/or the editor(s). MDPI and/or the editor(s) disclaim responsibility for any injury to people or property resulting from any ideas, methods, instructions or products referred to in the content.